Journal of Solid State Chemistry **162,** 34–41 (2001)
doi:10.1006/jssc.2001.9338, available online at http://www.idealibrary.com on IDEAL®

Calcium Insertion in the $Na_4Mn_9O_{18}$ Tunnel Structure: $Na_{1.1}Ca_{1.8}Mn_9O_{18}$

N. Floros, C. Michel, M. Hervieu, and B. Raveau

Laboratoire CRISMAT, UMR CNRS ISMRA 6508, 6 bd Maréchal Juin, 14050 Caen Cedex, France

Received April 5, 2001; in revised form July 19, 2001; accepted August 2, 2001

A new mixed valent manganese oxide, $Na_{1.1}Ca_{1.8}Mn_9O_{18}$, with a tunnel structure closely related to that of $Na_4Mn_9O_{18}$ has been synthesized. It crystallizes in the *Pnma* space group with $a = 26.418(2)$ Å, $b = 5.6468(4)$ Å, and $c = 9.1384(8)$ Å. Its structural study, combining X-ray powder diffraction and electron microscopy, shows that the $[Mn_9O_{18}]_\infty$ framework is similar to that of $Na_4Mn_9O_{18}$, forming large S-shaped and six-sided tunnels running along b. In contrast, the positions and distributions of calcium in the tunnels are different from those obtained for sodium in $Na_4Mn_9O_{18}$, explaining the doubling of the periodicity along the tunnel axis direction. The insulating properties of these oxides agree with a tendency to ordering of the Mn^{3+} and Mn^{4+} species in different sites. © 2001 Academic Press

INTRODUCTION

The investigations carried out on manganese oxides in past years have shown that the mixed valence of manganese is susceptible to playing an important role in the physical properties of those materials and may be the key for the discovery and control of new properties. This is exemplified by the spinel $LiMn_2O_4$ family, which is studied as a positive electrode in lithium ion batteries, and by the perovskite manganites $Ln_{1-x}A_xMnO_3$, which exhibit colossal magnetoresistance properties. In this respect, the manganese oxides with the formulation A_xMnO_2, where A is a divalent or univalent cation (Ba^{2+}, Pb^{2+}, K^+, Rb^+), represent an important family with the hollandite-type tunnel structure (1–5), or with closely related structures (6–7). With the same formulation, different types of tunnels can be formed, as shown for instance for $Ba_6Mn_{24}O_{48}$ (8) where hollandite-type columns coexist with rutile-type columns in the same structure.

The introduction of smaller A cations such as sodium induces the formation of different types of tunnels as illustrated by the structure of $Na_4Mn_9O_{18}$ (9), isotypic to $Na_4Mn_4Ti_5O_{18}$ (10), which consists of large S-shaped and of six-sided tunnels partially occupied by Na^+ cations. Calcium, owing to its size, close to that of sodium should be able to accommodate such a structure. We report herein on the structure and properties of a new mixed valent manganite, $Na_{1.1}Ca_{1.8}Mn_9O_{18}$, which exhibits a $[Mn_9O_{18}]_\infty$ framework similar to that of $Na_4Mn_9O_{18}$, but differs from the latter by a cationic deficiency and by an original distribution of calcium, sodium, and vacancies in the tunnels.

EXPERIMENTAL

The samples were prepared by solid state reaction, starting from CaO, MnO_2, and $NaMnO_2$ as precursors. Different mixtures were prepared, keeping nine as the total manganese amount but varying the ratio Ca/Na, according to $Na_{4-x}Ca_xMn_9O_{18+x}$. The mixtures were ground in an agate mortar, pressed in the form of bars, and sealed in evacuated silica tubes. They were heated at 1000°C for 8 h and slowly cooled down to room temperature.

The oxygen content was determined by chemical analyses using redox back titration. The X-ray powder diffraction (XRPD) data were collected at room temperature with a Philips diffractometer, working with the Cu$K\alpha$, in the range $10^\circ \leq 2\theta \leq 110^\circ$ in increments of 0.02° in 2θ. Data were analyzed by the Rietveld method using the computer program Fullprof (11).

Samples for transmission electron microscopy were prepared by crushing the bars in alcohol and the small crystallites in suspension were deposited onto a holey carbon film, supported by a copper grid. The electron diffraction (ED) study was carried out at room temperature with a JEOL 200CX electron microscope. High-resolution electron microscopy (HREM) was performed with a TOPCON 002B microscope with a point resolution of 1.7 Å. Energy-dispersive spectroscopy (EDS) analyses were systematically carried out, both electron microscopes being equipped with KEVEX analyzers.

The resistivity measurements were performed from room temperature down to 5 K by a classical four-probe method on sintered bars. The magnetization versus temperature was registered upon warming with a vibrating sample magnetometer in a magnetic field of 3000 G, which was applied at 5 K after zero-field cooling.

0022-4596/01 $35.00

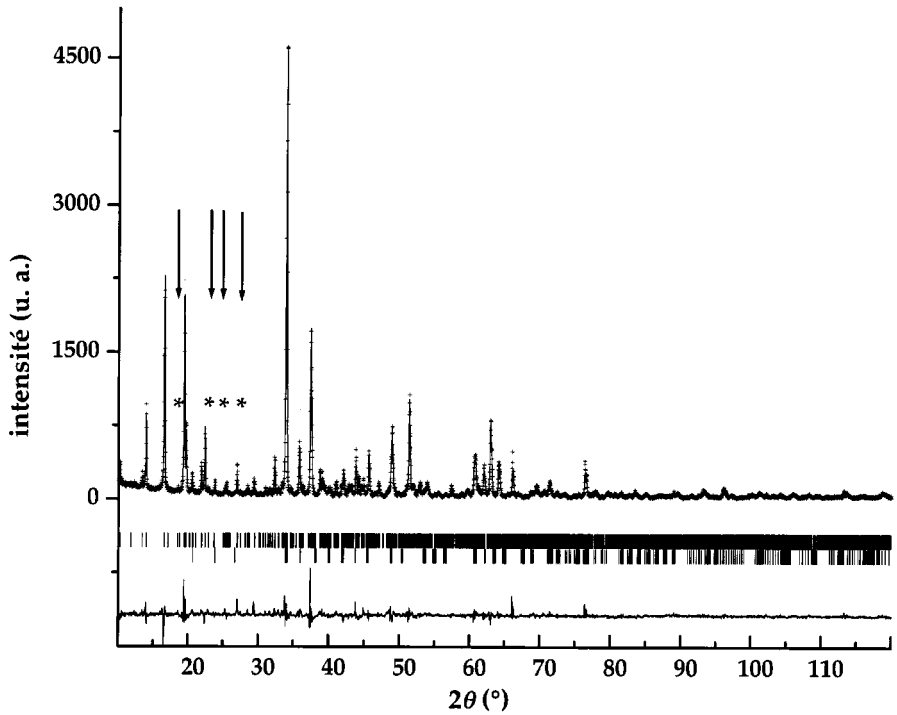

FIG. 1. X-ray powder diffraction patterns of $Na_{1.1}Ca_{1.8}Mn_9O_{18}$: dots (experimental); solid line (calculated and difference). Small vertical lines indicate Bragg angle position for the title phase (upper) and $CaMnO_{3-\delta}$ (lower). Vertical bars with star correspond to some of the diffraction peaks that cannot be indexed with $b \approx 2.8$ Å.

RESULTS AND DISCUSSION

According to the experimental process, a practically pure compound was synthesized for $x = 1.8$. The average cation content, determined by EDS analyses carried out on numerous crystallites, is close to "$Na_{1.1}Ca_{1.8}Mn_9$" (calculated for nine Mn atoms per unit), showing that sodium loss in the compound cannot be avoided in spite of the use of a sealed silica tube. Based on these results and the chemical analyses, the formulation of the compound is $Na_{1.1}Ca_{1.8}Mn_9O_{18}$. The X-ray powder diffraction pattern of this phase (Fig. 1) shows its isotypism with $Na_4Mn_9O_{18}$; nevertheless, some weak diffraction peaks can only be indexed considering the doubling of the one parameter is involved with respect to $Na_4Mn_9O_{18}$ or to $Na_4Mn_4Ti_5O_{18}$, i.e., $b_{Na_{1.1}Ca_{1.8}} \approx 2c_{Na_4}$. The electron diffraction study confirms the above statement. Reconstructing the reciprocal space by tilting around the crystallographic axes shows an orthorhombic cell, whose parameters, refined from XRD data, are $a = 26.418(2)$ Å, $b = 5.6468(4)$ Å, and $c = 9.1384(8)$ Å for $Na_{1.1}Ca_{1.8}Mn_9O_{18}$, to be compared with $a = 9.268(5)$ Å, $b = 26.601(5)$ Å, and $c = 2.882(2)$ Å for $Na_4Mn_4Ti_5O_{18}$ (10). The conditions limiting the reflection are $hk0: h = 2n$ and $0kl: k + l = 2n$, involving *Pnma* and $Pn2_1a$ as possible space groups. The [001] and [010] ED patterns are given in Fig. 2. The a and c parameters are close to those expected for the tunnel structure, and a doubling of the b parameter (periodicity along the tunnel) is observed, as shown by the rather intense additional reflections indicated by the white arrows in Fig. 2b.

The high-resolution electron microscopy study was carried out, selecting the [010] orientation to understand the polyhedra arrangement in the host lattice. Three images of the experimental through focus series are given in Fig. 3. For $\Delta f = -25$ nm (Fig. 3a), close to the Scherzer value, the heavy electron density zones appear as dark spots and for $\Delta f = -55$ nm (Fig. 3b), they are bright spots. Such a contrast is consistent with a tunnel structure similar to that observed for $Na_4Mn_4Ti_5O_{18}$ (10). Based on the electron diffraction and HREM observations, calculations were carried out using XRPD data, in the space group *Pnma*, taking into consideration the structural results obtained for $Na_4Ti_5Mn_4O_{18}$ in the *Pbam* space group (10], with the parameter relationships: $a_{Pnma} \approx b_{Pbam}$ and $c_{Pnma} \approx a_{Pbam}$. $CaMnO_{3-\delta}$, which was detected as an impurity, was introduced in the calculations as a secondary phase. Due to the large number of independent atoms (25), which implies too numerous variable parameters, thermal factors were fixed arbitrarily to 1.5 Å^2 for all the oxygen atoms, and the same B factor was assigned for all Mn atoms, for all Ca, and for all Na atoms, respectively (see Table 1).

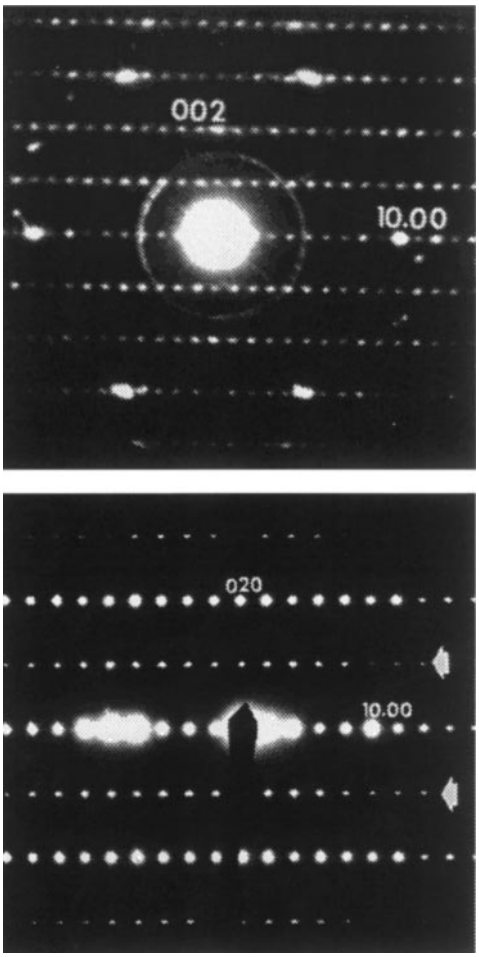

FIG. 2. [001] and [010] ED patterns of $Na_{1.1}Ca_{1.8}Mn_9O_{18}$.

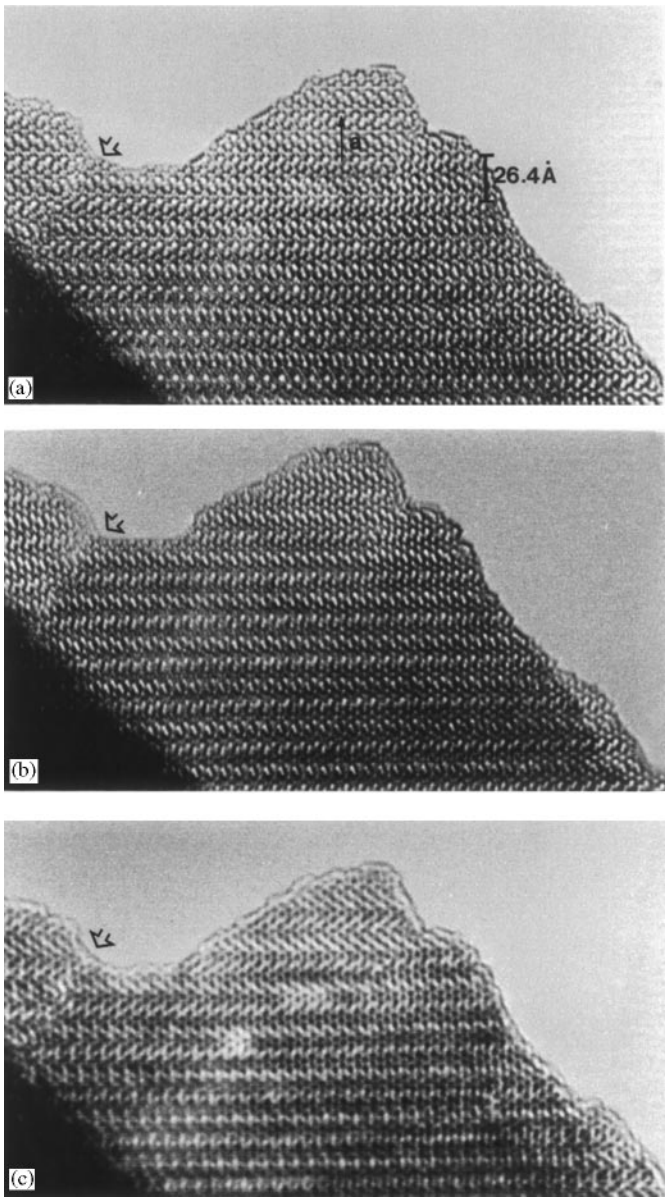

FIG. 3. [010] HREM images for focus values close to (a) -25 nm, (b) -55 nm, and (c) -85 nm.

Positional parameters of cations were first refined, considering different distributions of calcium and sodium in the structure (the total "$Na_{1.1}Ca_{1.8}$" cationic composition was assimilated in a first step to "Ca_3"), keeping the oxygen positions fixed. Then, oxygen positions were refined. During the refinements, it was observed that, considering partial occupancy of all the tunnel sites by calcium ions, two 8*g* sites were 50% occupied, whereas the two other 4*c* sites were less than 65% occupied. If one admits that the 8*g* sites are occupied by calcium and the 4*c* sites by sodium, this refinement of the occupancy factors of the tunnel sites leads to the composition $Na_{1.25}Ca_2Mn_9O_{18}$, close to the EDS analysis ($Na_{1.1}Ca_{1.8}Mn_9O_{18}$). Starting from this cationic distribution, positional parameters of metallic elements and oxygen atoms and the thermal factors and occupancy factors of calcium and sodium sites were successively refined. Convergence was reached for the atomic parameters listed in Table 1. The *R* factors, $R_p = 10.9\%$, $R_{w_p} = 15.0\%$ and $R_i = 8.7\%$, show that the refinement is consistent with the structural model. Nevertheless, these calculations cannot be considered as accurate due to the large number of variables compared to the limited amount of information from X-ray powder diffraction data. Coming back to the observed HREM images, simulations of these images were carried out using the atomic coordinates obtained from XRPD refinements. The three theoretical images, calculated for the positional parameters listed in Table 1, for $\Delta f = -25$, -55, and -85 nm and a crystal thickness of 24 Å, are given in Fig. 4a. They fit with the experimental ones displayed in Fig. 3. Black arrowheads indicate the Ca atoms surrounded by four MnO_6 octahedra and two MnO_5 pyramids. The theoretical image obtained for $\Delta f = -25$ nm is enlarged in Fig. 4b. The very dark spots are correlated to the Mn

TABLE 1
Refined Parameters for $Na_{1.1}Ca_{1.8}Mn_9O_{18}$: Space Group *Pnma*, $a = 26.419(2)$ Å, $b = 5.6466(2)$ Å, $c = 9.1385(4)$ Å

Atom	Site	x	y	z	B (Å^2)	n
Mn(1)	4*b*	0.0	0.0	0.5	1.09(6)	4
Mn(2)	4*c*	0.3064(7)	0.25	0.362(2)	1.09(6)	4
Mn(3)	4*c*	0.6939(7)	0.25	0.649(2)	1.09(6)	4
Mn(4)	8*d*	0.1067(2)	− 0.004(2)	0.0120(7)	1.09(6)	8
Mn(5)	8*d*	0.3021(3)	0.014(3)	0.0445(6)	1.09(6)	8
Mn(6)	4*c*	0.0942(6)	0.25	0.374(2)	1.09(6)	4
Mn(7)	4*c*	0.9110(6)	0.25	0.638(2)	1.09(6)	4
Ca(1)	8*d*	0.1999(8)	0.042(3)	0.218(1)	0.6(2)	4
Ca(2)	8*d*	0.0029(6)	0.043(4)	0.118(2)	0.6(2)	4
Na(1)	4*c*	0.4124(8)	0.25	0.203(2)	1.4(3)	2.5(1)
Na(2)	4*c*	0.5876(8)	0.25	0.797(2)	1.4(3)	2.5(1)
O(1)	8*d*	0.0992(8)	0.0[a]	0.259(2)	1.5(2)	8
O(2)	8*d*	0.2715(7)	0.0[a]	0.416(2)	1.5(2)	8
O(3)	8*d*	0.3509(8)	0.0[a]	0.304(2)	1.5(2)	8
O(4)	8*d*	0.0739(8)	0.0[a]	0.506(2)	1.5(2)	8
O(5)	4*c*	0.0016(8)	0.25	0.362(2)	1.5(2)	4
O(6)	4*c*	0.9984(8)	0.25	0.638(2)	1.5(2)	4
O(7)	4*c*	0.1604(8)	0.25	0.035(2)	1.5(2)	4
O(8)	4*c*	0.8396(8)	0.25	0.965(2)	1.5(2)	4
O(9)	4*c*	0.1746(7)	0.25	0.431(2)	1.5(2)	4
O(10)	4*c*	0.8254(7)	0.25	0.569(2)	1.5(2)	4
O(11)	4*c*	0.2776(8)	0.25	0.163(2)	1.5(2)	4
O(12)	4*c*	0.7224(8)	0.25	0.837(2)	1.5(2)	4
O(13)	4*c*	0.5633(8)	0.25	0.530(2)	1.5(2)	4
O(14)	4*c*	0.4367(8)	0.25	0.470(2)	1.5(2)	4

Note. $R_p = 10.9\%$, $R_{wp} = 15.0\%$, $R_i = 8.7\%$.
For $i = 5, 7, 9, 11, 13$: $x_{O(i+1)} = -x_{O(i)}$, $z_{O(i+1)} = -z_{O(i)}$.
[a] Parameters not refined.

positions (black arrow) and the positions of the cations located in the tunnels of the structure are indicated by black and white arrowheads.

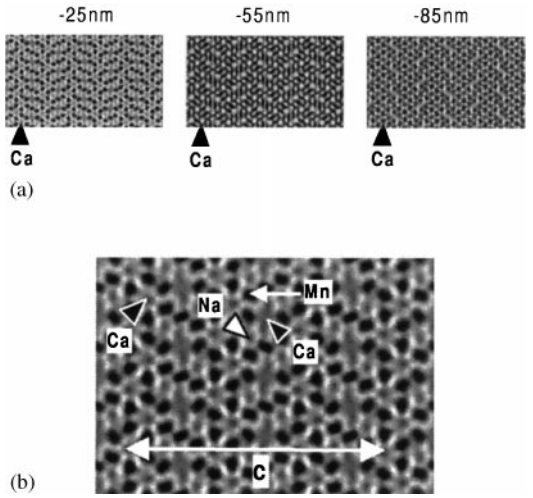

FIG. 4. (a) Calculated [010] HREM images for − 25-, − 55-, and − 85-nm focus values (crystal thickness = 24 Å). (b) Enlarged [010] HREM calculated image for a focus value close to − 25 nm.

These results show that the structure of $Na_{1.1}Ca_{1.8}Mn_9O_{18}$ exhibits a $[Mn_9O_{18}]_\infty$ host lattice similar to that of $Na_4Mn_4Ti_5O_{18}$ (10). The projection of the structure along **b** (Fig. 5) shows indeed that the $[Mn_9O_{18}]_\infty$ framework is built up of rutile chains running along **b**, sharing the edges of their octahedra in the (*a*, *c*) plane to form triple and double octahedral ribbons. Each triple ribbon shares two apices with two double ribbons, whereas one double ribbon shares only one apex with one triple ribbon. These octahedral ribbons form layers parallel to (100) and interconnected by MnO_5 pyramids. It results in the formation of two kinds of tunnels running along **b**: large S-shaped tunnels and smaller six-sided tunnels. The interatomic Mn–O distances

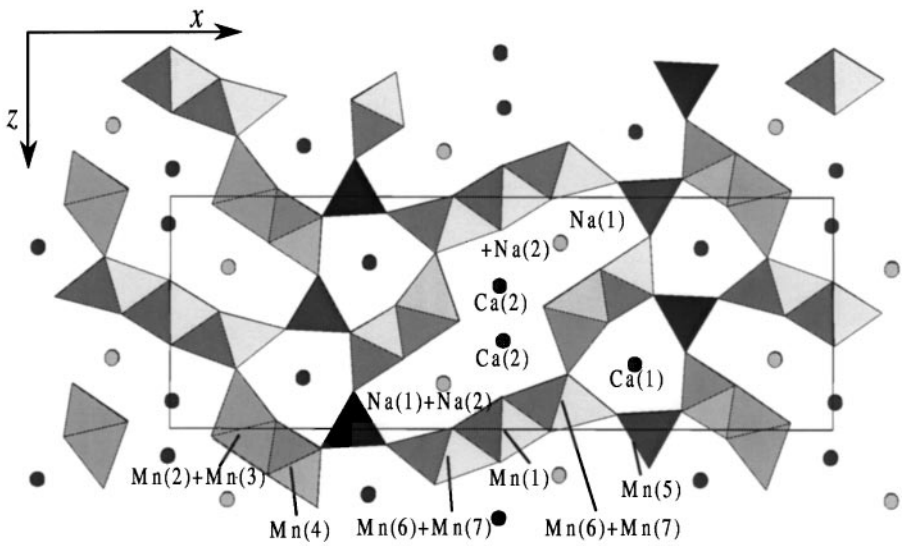

FIG. 5. [010] Projection of the structure of $Na_{1.1}Ca_{1.8}Mn_9O_{18}$.

TABLE 2
Interatomic Bond Distances

M–O	*d* (Å)	*M*–O	*d* (Å)
Mn(1)–O(4)	1.95(2) (×2)	Mn(7)–O(1)	1.72(2) (×2)
–O(5)	1.89(1) (×2)	–O(4)	1.97(2) (×2)
–O(6)	1.89(1) (×2)	–O(6)	2.31(3) (×1)
⟨Mean value⟩	1.91	–O(10)	2.35(3) (×1)
		⟨Mean value⟩	2.01
Mn(2)–O(2)	1.76(4) (×2)		
–O(3)	1.91(4) (×2)	Ca(1)–O(1)	2.70(3) (×1)
–O(8)	1.81(3) (×1)	–O(2)	2.63(3) (×1)
–O(11)	1.98(3) (×1)	–O(2)	2.87(3) (×1)
⟨Mean value⟩	1.85	–O(7)	2.29(2) (×1)
		–O(8)	2.57(2) (×1)
Mn(3)–O(2)	1.78(4) (×2)	–O(9)	2.37(2) (×1)
–O(3)	1.89(4) (×2)	–O(10)	2.64(2) (×1)
–O(7)	1.90(3) (×1)	–O(11)	2.42(3) (×1)
–O(12)	1.88(3) (×1)	–O(12)	2.68(3) (×1)
⟨Mean value⟩	1.85		
		Ca(2)–O(1)	2.86(3) (×1)
Mn(4)–O(1)	2.26(2) (×1)	–O(5)	2.52(2) (×1)
–O(3)	2.21(2) (×1)	–O(6)	2.78(2) (×1)
–O(7)	2.03(2) (×1)	–O(13)	2.54(2) (×1)
–O(8)	2.00(2) (×1)	–O(13)	2.40(2) (×1)
–O(13)	1.88(2) (×1)	–O(14)	2.67(2) (×1)
–O(14)	1.84(2) (×1)	–O(14)	2.25(2) (×1)
⟨Mean value⟩	2.04		
		Na(1)–O(3)	2.34(2) (×2)
Mn(5)–O(2)	2.27(2) (×1)	–O(4)	2.32(2) (×2)
–O(9)	1.92(2) (×1)	–O(5)	2.43(3) (×1)
–O(10)	1.79(2) (×1)	–O(14)	2.52(3) (×1)
–O(11)	1.83(2) (×1)		
–O(12)	1.95(2) (×1)	Na(2)–O(3)	2.34(3) (×2)
⟨Mean value⟩	1.95	–O(4)	2.32(4) (×2)
		–O(6)	2.43(3) (×1)
Mn(6)–O(1)	1.77(2) (×2)	–O(13)	2.52(3) (×1)
–O(4)	1.93(2) (×2)		
–O(5)	2.45(3) (×1)		
–O(9)	2.19(2) (×1)		
⟨Mean value⟩	2.01		

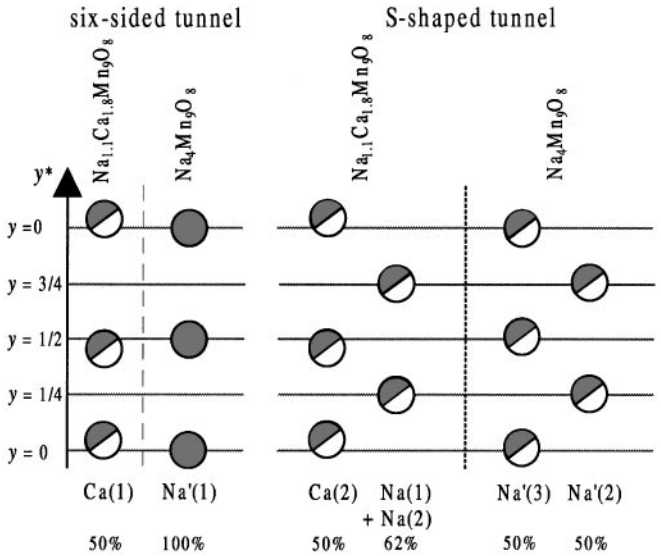

FIG. 6. Schematized representation of the cationic positions and distributions in the tunnels of $Na_{1.1}Ca_{1.8}Mn_9O_{18}$ and $Na_4Mn_4Ti_5O_{18}$ structures. *y* is refered to the *b* axis of $Na_{1.1}Ca_{1.8}Mn_9O_{18}$ structure. Ca(1), Ca(2), Na(1), and Na(2) are related to $Na_{1.1}Ca_{1.8}Mn_9O_{18}$ and Na′(1), Na′(2), and Na′(3) to $Na_4Mn_4Ti_5O_{18}$.

obtained for $Na_{1.1}Ca_{1.8}Mn_9O_{18}$ (Table 2), close to those observed for $Na_4Mn_4Ti_5O_{18}$ (10), confirm that the two frameworks $[Mn_9O_{18}]_\infty$ and $[Mn_4Ti_5O_{18}]_\infty$ are very similar.

The important difference between the two structures, $Na_{1.1}Ca_{1.8}Mn_9O_{18}$ and $Na_4Mn_4Ti_5O_{18}$, concerns the positions of the Na^+ and Ca^{2+} cations in the tunnels and their distribution. The latter are schematized on Fig. 6 for the sake of clarity. Considering first, the six-sided tunnels, it clearly appears that the periodicity along the tunnel axis between these cationic sites is different in the two structures. In $Na_4Mn_4Ti_5O_{18}$ two successive Na′(1) sites are spaced *b*/2 (taking the *b* axis of $Na_{1.1}Ca_{1.8}Mn_9O_{18}$ as a reference), along the tunnel axis, whereas in $Na_{1.1}Ca_{1.8}Mn_9O_{18}$, the corresponding Ca(1) sites are no more equidistant, two neighboring sites being brought closer together, leading to a *b* periodicity for the second one instead of *b*/2 for the first one. Moreover, the too small distance between two successive Ca(1) sites hinders their simultaneous occupation, explaining then maximum 50% occupancy by calcium, in contrast to the Na′(1) sites whose larger distances allow full occupancy by sodium. A similar phenomenon appears for the Ca(2) sites of the S-shaped tunnels, which are shifted in a similar way with respect to the corresponding Na′(3) sites of the $Na_4Mn_4Ti_5O_{18}$ structure and consequently cannot be more than 50% occupied by calcium due to the short distance between two successive sites along the tunnel axis. In contrast, the Na_1 and Na_2 sites of the $Na_{1.1}Ca_{1.8}Mn_9O_{18}$ structure exhibit positions similar to those of the corresponding Na'_2 sites of $Na_4Mn_4Ti_5O_{18}$, in agreement with the fact that, in both structures, those sites are only occupied by sodium; the slightly different occupancy factors for those Na(1) (60%), Na(2) (60%), and Na′(2) (50%) sites are all compatible with the distance *b*/2 between two successive sites, which allows a value up to 100% to be reached.

The very regular contrast observed at the level of the different atomic sites of the tunnels from HREM images (Fig. 3), whatever the focus value and the crystal thickness, suggests that the occupancy of these sites does not vary from one tunnel to the next. Image calculations show that the difference between one filled and one empty tunnel should be easily detectable; thus, the experimental and calculated contrasts are in agreement with the cationic distribution

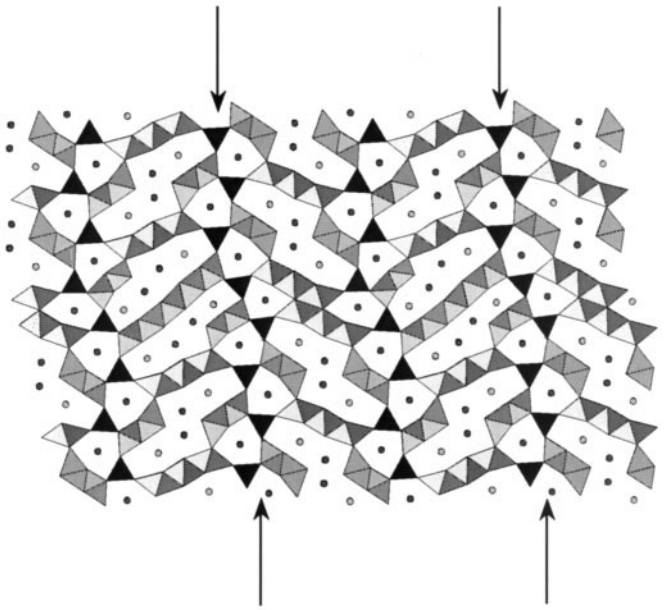

FIG. 7. Structural model of defect observed in HREM.

proposed from EDS analyses and XRPD refinements. Note also that the HREM images show a very regular arrangement of the octahedral ribbons. Only one type of defect is observed (see open arrow in Fig. 3), which can be detected by observation at grazing incidence. Such a defect, which involves a translation of the ribbons and tunnels (compare upper and lower parts of the image), results from the local presence of a larger octahedral ribbon built up of five edge-sharing rutile-type chains (Fig. 7), which can be rapidly compensated by the rearrangement of the surrounding ribbons.

This study confirms the ability of manganese to exhibit, in such structures, a mixed valency with an average oxidation state close to 3.5, like for $Na_4Mn_9O_{18}$, the tunnels being cationic deficient with respect to the latter. Such a mixed valency raises the question of a possible electronic delocalization in the $[Mn_9O_{18}]_\infty$ framework. The interatomic distances (Table 2) obtained from XRPD calculations, even if they are not accurate, suggest, in contrast, a tendency to the ordering Mn^{3+} and Mn^{4+} species: Mn(1), Mn(2), and Mn(3) sites, which exhibit small Mn–O bonds, smaller than 1.95 Å, should be only occupied by Mn^{4+} cations, whereas Mn(4), Mn(5), Mn(6), and Mn(7) sites, for which Mn–O distances larger than 2.2 Å are observed, should be preferentially occupied by Mn^{3+} species ($\frac{2}{3}Mn^{3+} + \frac{1}{3}Mn^{4+}$). Such a distribution should prevent any electronic delocalization. The transport properties of this manganite confirm this viewpoint. The room-temperature resistivity is rather high ($\rho = 2.5 \times 10^4$ Ω-cm) and increases rapidly as the temperature decreases (Fig. 8), becoming too high to be measured below 220 K. The plot Ln $\rho = f(T^1)$, in the range 220–360 K (inset Fig. 8) is linear, showing that the thermal variation of the resistivity obeys the equation $\rho = \rho_0 e^{E_a/kT}$, with $E_a = 0.33$ eV. This behavior is very similar to those

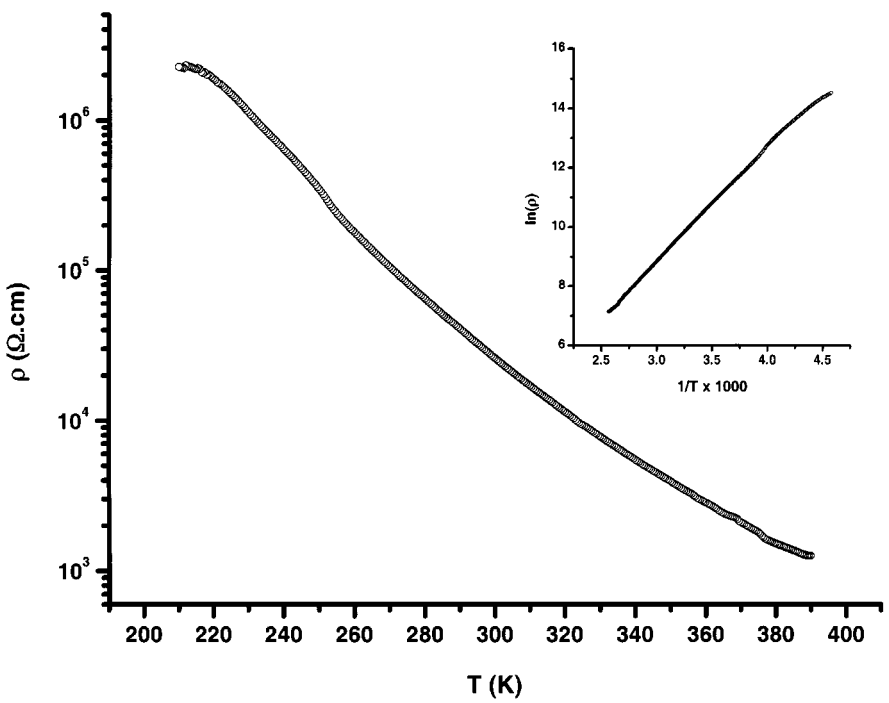

FIG. 8. Temperature-dependent resistivity in $Na_{1.1}Ca_{1.8}Mn_9O_{18}$.

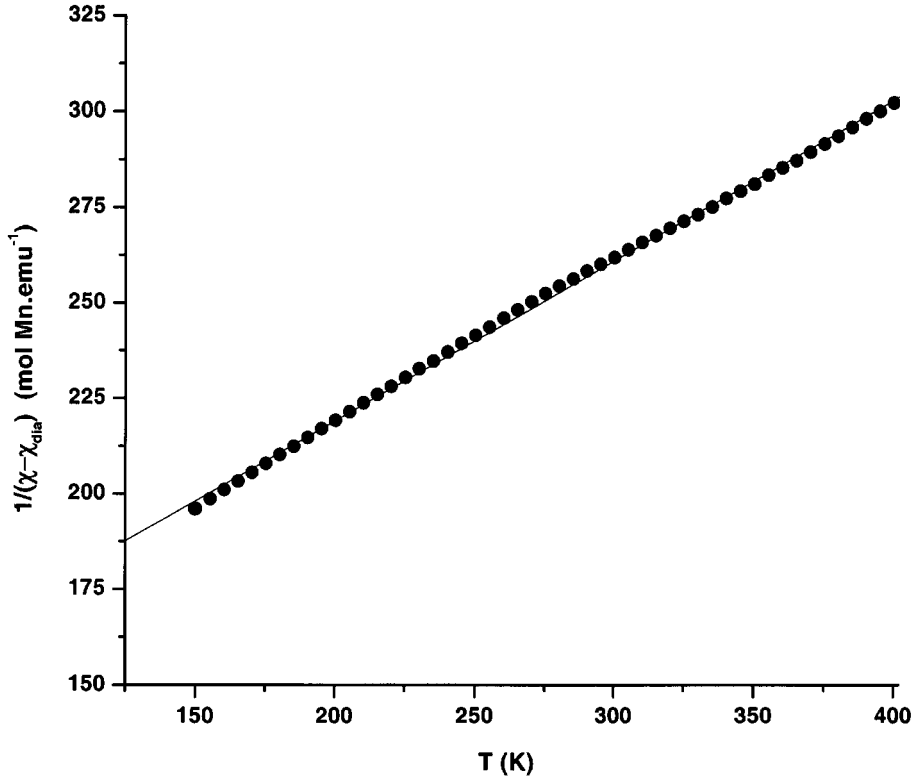

FIG. 9. Temperature dependence of χ_M^{-1} for $Na_{1.1}Ca_{1.8}Mn_9O_{18}$.

observed for γMnO_2 (12) and $Na_4Mn_9O_{18}$ (10), which exhibit E_a values of 0.35 and 0.28 eV and resistivity values at 293 K of 4.4×10^3 and 2×10^3 Ω-cm, respectively. In such edge-sharing octahedra conduction should mainly occur through direct exchange by direct overlapping of the d orbitals of manganese. Such an overlapping is only possible if the Mn–Mn distance is smaller than a critical distance, d_c, which can be calculated using the equation proposed by Goodenough (13) for a 3d cation: $d_c^{n+} = 3.2 - 0.05n - 0.03(Z - Z_{Ti}) - 0.04S(S+1)$, where n is the charge, Z the atomic number, and S the total spin. For Mn^{3+} and Mn^{4+}, d_c is 2.72 and 2.76 Å, respectively. These values are smaller than the Mn–Mn distance along c observed in these three compounds and could explain their insulating character.

Finally, the magnetic susceptibility as a function of the temperature has been measured under a 3000 G field. The compound exhibits paramagnetic behavior in the range of 130–400 K and follows a Curie–Weiss law (Fig. 9). The fitting of the $\chi_M^{-1}(T)$ curve leads to an effective magnetic moment of $4.36\mu_B$ per manganese and θ_P of -320 K. This negative value of θ_P supports the existence of strong antiferromagnetic interactions in this oxide. The value of $4.36\mu_B$ is close to the theorical magnetic moment obtained for a composition of 50% Mn^{3+} and 50% Mn^{4+} ($= 4.39\mu_B$). The presence of $CaMnO_{3-\delta}$ as a secondary phase does not disturb the signal in the paramagnetic domain since it represents approximately 1% in weight in the sample and because the $CaMnO_{3-\delta}$ paramagnetic state is observed above $T_N = 122$ K (14). In contrast, the presence of $CaMnO_{3-\delta}$ prevents any interpretation of the magnetic susceptibility below 122 K.

In conclusion, a novel manganite closely related to $Na_4Mn_9O_{18}$ has been synthesized, which differs mainly from the latter by cationic deficiency and by the distribution and positions of calcium and sodium in the tunnels. It appears clearly that the introduction of calcium induces the appearance of different types of sites, which are shifted with respect to the previous sodium sites, implying a doubling of the periodicity along the tunnel axis and characterized by a maximum occupancy factor of 50% due to their too short distances. The tendency of Mn^{3+} and Mn^{4+} species to order, shown from the interatomic distances, is in agreement with the insulating properties of this phase in spite of the apparent mixed valency of manganese. The insertion of various cations on the sodium sites of $Na_4Mn_9O_{18}$ should allow new types of cationic orderings to be evidenced in the future.

REFERENCES

1. A. Byström and A. M. Byström, *Acta Crystallogr.* **3,** 146 (1950).
2. G. Butler and H. R. Thusk, *Acta Crystallogr.* **5,** 288 (1952).
3. A. Byström and A. M. Byström, *J. Solid State Chem.* **3,** 323 (1971).

4. R. W. Cheary, *Acta Crystallogr.* **46,** 599 (1990).
5. C. Fouassier, C. Delmas, and P. Hagenmuller, *Mater. Res. Bull.* **10,** 443 (1993).
6. A. D. Wadsley, *Acta Crystallogr.* **6,** 433 (1963).
7. L. C. Nestor, G. Van Tendeloo, and S. Amelinckx, *J. Solid State Chem.* **109,** 152 (1994).
8. Ph. Boullay, M. Hervieu, and B. Raveau, *J. Solid State Chem.* **132,** 239 (1997).
9. J. P. Parant, R. Olazcagova, M. Devalette, C. Fouassier, and P. Hagenmuller, *J. Solid State Chem.* **3,** 1 (1971).
10. W. G. Mumme, *Acta Crystallogr. B* **24,** 1114 (1968).
11. J. Rodriguez-Carjaval, "Abstracts of Satellite Meeting on Power Diffraction of XVth Congr. Int. Union of Crystallography, Toulouse," p. 127. 1990.
12. J. P. Chevillot and J. Brenet, *C. R. Acad Sci. Paris* **76** (1959).
13. J. B. Goodenough, "Metallic Oxides." Pergamon, Elmsford, NY, 1971.
14. A. Maignan, C. Martin, F. Damay, and B. Raveau, *Phys. Rev. B.* **58,** 2758 (1998).